



HAL
open science

SN 1885A and Supernova Remnants in the Centre of M31 with LOFAR

Deepika Venkattu, Peter Lundqvist, Miguel Pérez Torres, Etienne Bonnassieux, Cyril Tasse, Anne-Laure Melchior, Francoise Combes

► **To cite this version:**

Deepika Venkattu, Peter Lundqvist, Miguel Pérez Torres, Etienne Bonnassieux, Cyril Tasse, et al.. SN 1885A and Supernova Remnants in the Centre of M31 with LOFAR. *The Astrophysical Journal*, 2024, 976, 10.3847/1538-4357/ad890f . insu-04808506

HAL Id: insu-04808506

<https://insu.hal.science/insu-04808506v1>

Submitted on 28 Nov 2024

HAL is a multi-disciplinary open access archive for the deposit and dissemination of scientific research documents, whether they are published or not. The documents may come from teaching and research institutions in France or abroad, or from public or private research centers.

L'archive ouverte pluridisciplinaire **HAL**, est destinée au dépôt et à la diffusion de documents scientifiques de niveau recherche, publiés ou non, émanant des établissements d'enseignement et de recherche français ou étrangers, des laboratoires publics ou privés.



Distributed under a Creative Commons Attribution 4.0 International License



SN 1885A and Supernova Remnants in the Centre of M31 with LOFAR

Deepika Venkattu¹ , Peter Lundqvist¹ , Miguel Pérez Torres^{2,3} , Etienne Bonnasieux^{4,5,6} , Cyril Tasse^{7,8},
Anne-Laure Melchior⁹, and Francoise Combes¹⁰

¹ The Oskar Klein Centre, Department of Astronomy, Stockholm University, AlbaNova, SE-10691 Stockholm, Sweden; deepika.venkattu@astro.su.se

² Instituto de Astrofísica de Andalucía (IAA-CSIC), Glorieta de la Astronomía, s/n, E-18008 Granada, Spain

³ School of Sciences, European University Cyprus, Diogenes Street, Engomi, 1516 Nicosia, Cyprus

⁴ Julius-Maximilians-Universität Würzburg, Fakultät für Physik und Astronomie, Institut für Theoretische Physik und Astrophysik, Lehrstuhl für Astronomie, Emil-Fischer-Straße 31, D-97074 Würzburg, Germany

⁵ LESIA, Observatoire de Paris, PSL University, CNRS, Sorbonne University, Université Paris Diderot, Sorbonne Paris Cité, 5 place Jules Janssen, 92195 Meudon, France

⁶ INAF, Istituto di Radioastronomia, Via Piero Gobetti, 101, 40129 Bologna BO, Italy

⁷ GEPI & ORN, Observatoire de Paris, Université PSL, CNRS, 5 Place Jules Janssen, 92190 Meudon, France

⁸ Department of Physics & Electronics, Rhodes University, PO Box 94, Grahamstown, 6140, South Africa

⁹ LERMA, Observatoire de Paris, Sorbonne University, PSL University, CNRS, 75014, Paris, France

¹⁰ Observatoire de Paris, LERMA, Collège de France, CNRS, PSL University, Sorbonne University, 75014, Paris, France

Received 2024 July 9; revised 2024 October 3; accepted 2024 October 18; published 2024 November 25

Abstract

We present the first LOFAR image of the center of M31 at a frequency of 150 MHz. We clearly detect three supernova remnants, which, along with archival VLA data at 3 GHz and other published radio and X-ray data, allows us to characterize them in detail. Our observations also allow us to obtain upper limits of the historical SN 1885A, which is undetected even at a low frequency of 150 MHz. From analytical modeling, we find that SN 1885A will stay in its free-expansion phase for at least another couple of centuries. We find an upper limit of $n_{\text{H}} \lesssim 0.04 \text{ cm}^{-3}$ for the interstellar medium of SN 1885A, and that the SN ejecta density is not shallower than $\propto r^{-9}$ (on average). From the 2.6σ tentative detection in X-ray, our analysis shows that nonthermal emission is expected to dominate the SN 1885A emission. Comparing our results with those on G1.9+0.3, we find that it is likely that the asymmetries in G1.9+0.3 make it a more efficient radio and X-ray emitter than SN 1885A. For Braun 80, 95, and 101, the other remnants in this region, we estimate ages of 5200, 8100, and 13,100 yr, and shock speeds of 1150, 880, and 660 km s^{-1} , respectively. Based on this, the supernova rate in the central $0.5 \text{ kpc} \times 0.6 \text{ kpc}$ of M31 is at least one per ~ 3000 yr. We estimate radio spectral indices of -0.66 ± 0.05 , -0.37 ± 0.03 , and -0.50 ± 0.03 for the remnants, respectively, which match fairly well with previous studies.

Unified Astronomy Thesaurus concepts: [Radio continuum emission \(1340\)](#); [Galaxies \(573\)](#); [Supernova remnants \(1667\)](#)

1. Introduction

M31, as the nearest spiral galaxy at 785 kpc away (A. W. McConnachie et al. 2005), has been well-studied across multiple wavelengths. In the radio, dedicated surveys of M31 have been undertaken, such as 36W (J. E. V. Bystedt et al. 1984), 37W (R. A. M. Walterbos et al. 1985), R. Braun (1990) and J. D. Gelfand et al. (2004) surveys, in addition to VLBI studies of parts of it (eg., J. S. Morgan et al. 2013). These surveys have helped to build a census of all the radio sources in the galaxy, to understand the galaxy dynamics and also study individual sources that inform us about the past massive star population (e.g., supernova remnants (SNRs), pulsars, and pulsar wind nebulae) and current massive star population (H II regions) in M31.

Studying supernovae (SNe) and SNRs at radio wavelengths presents a picture of the synchrotron emission from these sources, helping us understand the interaction of the expanding ejecta with the surrounding circumstellar/interstellar matter and the nature of the progenitor stars. To study spatially resolved SNRs in great detail, galactic remnants with their large angular sizes on the sky are a natural target. However,

limitations include confusion and unreliable distance estimates. Studying SNRs in nearby galaxies is a good solution and M31 in the Local Group is one of these preferred targets given that it is 785 kpc away and is a spiral galaxy like the Milky Way. Many SNR studies in M31 have been performed in the optical (e.g., S. Dodorico et al. 1980; R. Braun & R. A. M. Walterbos 1993; E. A. Magnier et al. 1995) and a few in X-ray and radio as well (e.g., J. R. Dickel & S. D'Odorico 1984; R. Supper et al. 2001; T. J. Galvin & M. D. Filipovic 2014).

SN 1885A, discovered on 1885 August 20th, was the first extragalactic supernova observed. Although it was also one of the brightest observed extragalactic supernovae, as a sub-luminous Type Ia supernova, it was never detected in the radio. G. de Vaucouleurs & H. G. J. Corwin (1985) present a centennial review of SN 1885A, providing a definitive light curve and reexamining color and spectral observations pointing to its thermonuclear origins. There have been attempts in the past few decades to study the expanding ejecta of SN 1885A, and even though it has been more than a century after explosion, emission from the remnant at the site of SN 1885A has not been detected at any wavelength (e.g., R. A. Fesen et al. 1989; P. C. Crane et al. 1992; S. K. Sarbadhikary et al. 2019). The expanding ejecta, however, has been imaged in resonance-line *absorption* in the optical and UV wavelengths (R. A. Fesen et al. 1989, 2015, 2017). Along with SNR G1.9+0.3 in our Galaxy, SN 1885A is one of two likely Type Ia SNe that fill the



Original content from this work may be used under the terms of the [Creative Commons Attribution 4.0 licence](#). Any further distribution of this work must maintain attribution to the author(s) and the title of the work, journal citation and DOI.

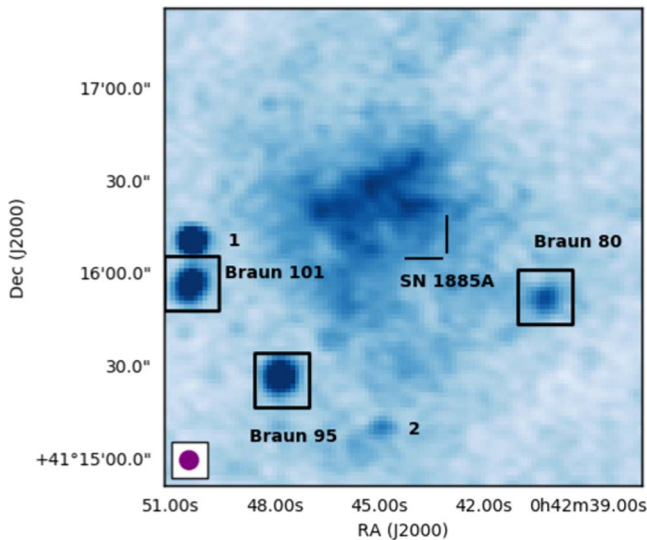


Figure 1. LOFAR image of the center of M31 at 150 MHz with Braun 80, 95, and 101 labeled and the position of SN 1885A marked. The bright source north of Braun 101 is GLG 001, and the source southwest of Braun 95 is M31N 2010-04a (marked 1 and 2, respectively; see also Table 4). The restoring beam is shown in the bottom left-hand corner.

gap in observations for our understanding of the SN–SNR transition phase.

For the first time, we present a Low Frequency Array (LOFAR; M. P. van Haarlem et al. 2013) image of the center of M31 and present fluxes for the three other SNRs in the region, and an upper limit for SN 1885A. We do not discuss M31* in this work because, along with a subarcsecond resolution study of M31, it is discussed in detail in E. Bonnassieux et al. (2024, in preparation). We focus only on the center of M31 covering three SNRs and SN 1885A in this work. Along with the LOFAR image, we include a Karl G. Jansky Very Large Array (VLA) image of the same region and include fluxes from other radio and X-ray studies of these four sources. Following the literature, in this work we refer to the three other SNRs as Braun 80, 95, and 101, as enumerated in the 1.4 GHz observations of R. Braun (1990).

In Section 2, we present the observations and source detection with LOFAR and VLA. In Section 3.1, we present radio modeling of SN 1885A in the context of the upper limits provided by our observations and the 6.2 GHz VLA image (S. K. Sarbadhicary et al. 2019). We discuss the X-ray upper limits in Section 3.1.2 and compare our results for SN 1885A with G1.9+0.3 in Section 3.1.3. Section 3.2 presents a discussion on morphology and spectra of the remnants Braun 80, 95, and 101 from radio and X-ray data available until date.

2. Observations

2.1. LOFAR

LOFAR data are obtained from project LC10_014 (PI: Dr. Anne-Laure Melchior) observed on 2018 September 17th (pointing P004+41). The observation using the High Band Antenna (HBA; 120–240 MHz) has a 10 minutes observation of a bright flux density calibrator (3C 196) after the 8 hr on-source observation. The data were recorded with 1 s sampling and in channels of 12.21 kHz width (16 channels per sub-band, 243 sub-bands). Data were reduced and imaged using the standard LINC¹¹

¹¹ <https://git.astron.nl/RD/LINC>

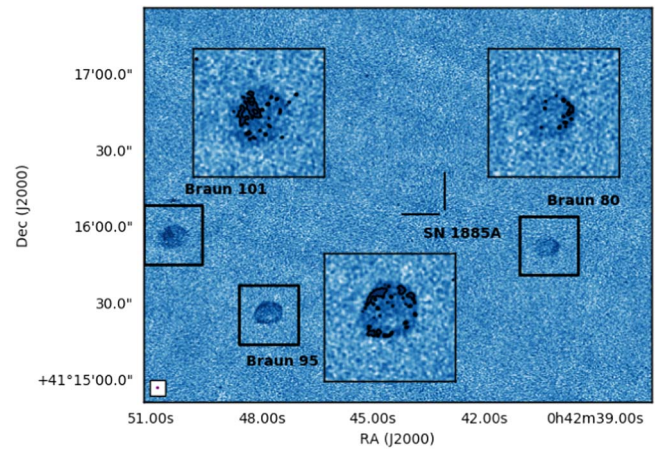


Figure 2. VLA image of center of M31 at 3 GHz with Braun 80, 95, and 101 labeled and the position of SN 1885A marked. The insets show the structure of the three remnants in greater detail. Bright point sources visible in this image are noted in Table 4. The restoring beam is shown in the bottom left-hand corner.

pipelines for direction-independent processing of the Dutch stations (formerly PREFACTOR; F. de Gasperin et al. 2019) followed by direction-dependent calibration and imaging using DDFacet (O. M. Smirnov & C. Tasse 2015; C. Tasse et al. 2018, 2023). The image, centered at 145 MHz, has a beam size of 6'' and rms of 0.1 mJy beam⁻¹ (Figure 1).

2.2. VLA

VLA data are obtained from project 22A-071 (PI: Dr. Zhiyuan Li) observed on 2022 June 27th. The C-band image centered at 3 GHz has a beam size of 0''.5 and rms of 3 μJy beam⁻¹ and was taken when the array was in A configuration. Data were processed through the VLA Calibration Pipeline with the flux calibrator 3C48 and the complex gain calibrator J0038+4137 and imaged with a Briggs weighting of 0.5 (Figure 2).

In addition to the data at 150 MHz and 3 GHz, we use previously published data in radio and X-ray from R. Braun (1990), L. O. Sjouwerman & J. R. Dickel (2001), A. K. H. Kong et al. (2003), S. K. Sarbadhicary et al. (2019), and F. Hofmann et al. (2013), as given in Tables 1, 2, and 3.

2.3. Source Detection

In the LOFAR image, the remnants Braun 80, 95, and 101 remain barely resolved, show no detailed structure, but are slightly bigger than the image beam. For this image, we use the default parameters for point sources in PYBDSF. There is a significant extended emission from this central region in the LOFAR image, and no clear emission that can be isolated as coming from SN 1885A itself. For a 6'' region centered on SN 1885A, we get a flux density of 0.797 mJy, which we treat as an upper limit for the source at 150 MHz.

For the VLA S-band image, where the remnants are resolved, we use the IMFIT function in CASA. The fit parameters for both images are given in Table 1. Although we do not discuss them further, we also add other point sources seen in the two images in Table 4 characterized with PYBDSF.

Table 1
SNRs in the M31 Core—Radio Fluxes

SNR	R.A.	Decl.	Central Frequency (GHz)	Integrated Flux Density (mJy)	Major (arcsec)	Minor (arcsec)	PA (deg)	Source
Braun 80	00 ^h 42 ^m 40 ^s .26	41 ^d 15 ^m 52 ^s .1	0.145	8.3 ± 1.4	14.11 ± 2.14	11.02 ± 1.52	97.85 ± 28.68	This work
			0.145	6.5 ± 1.5	10.64 ± 1.94	8.79 ± 1.4	121.7 ± 41.4	LoTSS ^a
			1.4	3.12 ± 0.46	21.17 ± 1.54	15.95 ± 1.11	156.0 ± 15.2	(1)
			3	0.62 ± 0.10	6.17 ± 1.02	5.55 ± 0.92	83 ± 63	This work
			8.4	0.53 ± 0.03 ^b	8.0	8.0	...	(2)
Braun 95	00 ^h 42 ^m 47 ^s .82	41 ^d 15 ^m 25 ^s .07	0.145	11.27 ± 1.19	10.50 ± 0.86	10.09 ± 0.81	162.05 ± 85.32	This work
			0.145	10.7 ± 1.7	11.68 ± 1.49	9.29 ± 1.05	107.19 ± 24.6	LoTSS ^a
			1.4	2.48 ± 0.19	9.79 ± 0.25	7.17 ± 0.27	108.3 ± 5.1	(1)
			3	1.03 ± 0.11	6.76 ± 0.73	5.92 ± 0.64	142 ± 33	This work
			8.4	1.41 ± 0.05 ^b	9.6	8.0	137	(2)
Braun 101	00 ^h 42 ^m 50 ^s .41	41 ^d 15 ^m 56 ^s .4	0.145	9.74 ± 0.9	10.34 ± 0.79	8.55 ± 0.58	146.05 ± 17.54	This work
			0.145	14.5 ± 2.0	13.9 ± 1.68	10.99 ± 1.2	0.12 ± 23.2	LoTSS ^a
			1.4	2.97 ± 0.23	10.93 ± 0.34	7.77 ± 0.53	133.9 ± 6.9	(1)
			3	1.14 ± 0.10	6.24 ± 0.55	5.52 ± 0.49	169 ± 29	This work
			4.9	1.13 ± 0.05 ^c	11.6	8.4	...	(3)
			8.4	1.29 ± 0.05 ^b	11.6	8.4	143	(2)

Notes.

^a https://vo.astron.nl/lotss_dr2/q/src_cone/form.

^b We add 3% error in addition to the 3σ from rms noise of 4 μ Jy reported in (2).

^c We add 3% error in addition to the 3σ from rms noise of 5 μ Jy reported in (3).

References: (1) R. Braun (1990); (2) L. O. Sjouwerman & J. R. Dickel (2001); (3) A. K. H. Kong et al. (2003).

Table 2
SNRs in the M31 Core: X-Ray Data

SNR	X-Ray Energy Band (keV)	Luminosity ($\times 10^{35}$ erg s^{-1})	Source
Braun 80	0.2–10	3.2	Estimated using (1)
Braun 95	0.2–10	5.3	Estimated using (1)
	0.3–7	8 ^{+7.0} _{-2.2}	(2)
Braun 101	0.2–10	6.2 ± 0.49	(1)
	0.3–7	4.4 ^{+1.3} _{-2.2}	(2)
	0.2–4.5	6.0 ± 0.51	Source 1050 in (3)
	0.35–2.0	12	XMMM31 J004250.47 +411556.7 in (4)

References: (1) F. Hofmann et al. (2013); (2) A. K. H. Kong et al. (2003); (3) H. Stiele et al. (2011); (4) M. Sasaki et al. (2012).

3. Discussion

3.1. SN 1885A

Radio observations of SN 1885A have so far been unsuccessful in detecting any emission (e.g., G. G. Pooley & S. Kenderdine 1967; J. R. Dickel & S. D’Odorico 1984; P. C. Crane et al. 1992). S. K. Sarbadhary et al. (2019) obtain the deepest radio image at the site of SN 1885A by coadding archival VLA observations between 4 and 8 GHz. They provide a 3σ upper limit of $<11.4 \mu\text{Jy beam}^{-1}$ at a central frequency of 6.2 GHz at 127 yr. We note here that although we use the term “SN 1885A” for uniformity with literature, the source is in its remnant phase and the discussion that follows also concerns the remnant “SNR 1885A.”

Observations in the UV and optical by R. A. Fesen et al. (1989, 2015, 2017) show evidence for expanding debris at the position of SN 1885A from resonance-line absorption against the background emission from M31. The fastest material has a

velocity of $\approx 13,400 \text{ km s}^{-1}$, as revealed by Ca I $\lambda 4227$ data from 2013 (R. A. Fesen et al. 2017). R. A. Fesen et al. (2017) compare the observationally inferred velocity structure of the debris with that of a subluminescent Type Ia SN model named 5p02822.16 by P. Höflich et al. (2002), and find qualitative similarities, enough to suggest that SN 1885A was the result of an off-center delayed-detonation explosion. In particular, Ca is present in the model out to $\approx 13,000 \text{ km s}^{-1}$. In the model there is also Si, S, and especially Mg present out to $\approx 18,000 \text{ km s}^{-1}$, with little or no mixing between Ca and Mg. R. A. Fesen et al. (2017) did not find any observational evidence of Mg at velocities $\gtrsim 13,000 \text{ km s}^{-1}$ which could signal a difference between the model and the observations. Or, it could be that ejecta with velocity originally greater than $\approx 13,400 \text{ km s}^{-1}$ could have been swept up by the reverse shock created by SN ejecta–ISM interaction, by the time of the observations in 2013 (at the age of 128 yr for SN 1885A). We suppose the latter to be the case.

To model the SN ejecta, we assume that the ejecta are spherically symmetric and expand in a homologous fashion, i.e., $V(r, t) = r/t$, where V is the velocity, r the radius, and t the time since explosion. We will use cgs units unless otherwise stated. We further presume that the ejecta density structure can be approximated by two power laws, where the inner structure is characterized by the density profile $\rho_i(V, t) \propto V^{-a} t^{-3}$ and the outer structure by $\rho_o(V, t) \propto V^{-n} t^{-3}$. The break in density slope between these two parts of the ejecta occurs at the velocity V_b , which can be calculated by integrating the density and kinetic energy profiles across the ejecta, to become

$$V_b = 10\,030 \sqrt{\frac{E_{51} (n-5)(5-a)}{M (n-3)(3-a)}} \text{ km s}^{-1}. \quad (1)$$

Here, E_{51} is the total kinetic energy of the ejecta in 10^{51} erg and M is the total ejecta mass in solar masses (see also R. A. Chevalier & C. Fransson 1994). Typical parameters for a Type Ia SN explosion

Table 3
SN 1885A: Radio and X-Ray Limits

SNR	Age (yr)	Central Frequency/X-Ray Energy Band (GHz/keV ⁻¹)	Integrated Flux Density (mJy)	Luminosity (erg s ⁻¹ Hz ⁻¹)	Source
SN 1885A	133	0.15 GHz	< 0.8	< 3.46 × 10 ²³	This work
	127	6.2 GHz	< 0.01	< 8.43 × 10 ²¹	(1)
	123	0.2-10 keV	...	< 2.0 × 10 ³⁴	(2)
	123	0.3-7 keV	...	< 1.6 × 10 ³⁴	Estimated using (2) and (3)

References: (1) S. K. Sarbadhicary et al. (2019); (2) F. Hofmann et al. (2013); (3) A. K. H. Kong et al. (2003).

are $E_{51} = 1$ and $M = 1.4 M_{\odot}$, and an oft-used value for n is $n = 10$ (e.g., J. K. Truelove & C. F. McKee 1999), although $n = 12$ – 14 have also been used for the outermost ejecta (e.g., E. Kundu et al. 2017). For the parameter a , the model 5p02822.16 indicates a value of 0–1 (see Figure 15 of R. A. Fesen et al. 2017), and the combination $E_{51} = 1$, $M = 1.4 M_{\odot}$, $n = 10$, and $a = 0$ (1) gives $V_b \approx 9250$ (10,100) km s⁻¹. In the model 5p02822.16 there is indeed a break in density at ~ 9000 km s⁻¹, but the density slope exterior to this velocity is shallower than $n = 10$ out to $\sim 23,000$ km s⁻¹. It is more like the $n = 7$ scenario discussed by R. A. Chevalier (1982) for Type I SNe. However, a steeper density slope could be expected for the ejecta with the highest velocities (see, e.g., V. V. Dwarkadas & R. A. Chevalier 1998 and E. Kundu et al. 2017). We use the a -values 0 and 1, and n -values between 7 and 12 as approximations to the full density profile. S. K. Sarbadhicary et al. (2019) used $a = 0$ and $n = 10$ in their models for SN 1885A. Our models M1–M8 are summarized in Table 5.

The fact that SN 1885A was subluminal (e.g., W. Huggins & W. F. Denning 1885; E. W. Maunder 1885; E. W. Maunder 1886; R. A. Chevalier & P. C. Plait 1988) may argue for $E_{51} \lesssim 1$. However, since there is no clear correlation between explosion energy and production of ⁵⁶Ni in the delayed-detonation scenario (see P. Höflich et al. 2002), we select a value of E for each combination of a and n so that the break in density structure occurs at ≈ 9000 km s⁻¹. In the 5p02822.16 model by P. Höflich et al. (2002), $E_{51} \approx 1.106$ (P. Höflich 2024, private communication), which is close to that in our models M2 and M8. The ejecta mass is fixed at $M = 1.4 M_{\odot}$.

As the SN ejecta expand, they will interact with the ISM. For a helium-to-hydrogen ratio (by number) of $n_{\text{He}}/n_{\text{H}} = 0.1$, the density of the ISM is $\rho_{\text{ISM}} = 1.4 m_p n_{\text{H}}$, where n_{H} is the hydrogen density in cm⁻³. The interaction between the ejecta and the ISM creates two shock waves, a forward one moving into the ISM, and a reverse shock moving into the ejecta. Since we assume a power-law density structure of the ejecta, and that the ISM density has a constant value, the shock structure can be obtained from the similarity solutions of R. A. Chevalier (1982), as long as the velocity of the outermost ejecta $V_{\text{ej,max}} \geq V_b$ and $n > 5$. Time t_b occurs when $V_{\text{ej,max}} = V_b$ and is simply $t_b = R_2(t_b)/V_b$, where $R_2(t_b)$ is the reverse shock radius at time t_b . As long as $t \leq t_b$, R_2 and R_1 (the radius of the forward shock) are related through $R_2 = R_1(R_2/R_c)(R_1/R_c)^{-1}$ where the ratios of R_1/R_c and R_2/R_c are tabulated in R. A. Chevalier (1982) for various values of n . Here, R_c is the radius of the contact discontinuity between shocked ejecta and shocked ISM. R_1 can be written as

$$R_1(t) = R_{1,128} \left(\frac{t_{\text{yr}}}{128} \right)^{(n-3)/n}, \quad (2)$$

where $R_{1,128}$ is the outer shock radius at 128 yr, i.e., at the time of the observations by R. A. Fesen et al. (2017), and t_{yr} is the time t since explosion in years.

We make use of the Ca I line analysis of R. A. Fesen et al. (2017), which shows that Ca I is present all the way out to 13,400 km s⁻¹. We therefore select $V_{\text{ej,max}}(128 \text{ yr}) = 13,400$ km s⁻¹ as the maximum ejecta velocity at 128 yr, corresponding to the reverse shock radius $R_{2,128} \approx 1.75$ pc (or a projected radius of 0".46 at a distance of 785 kpc). $R_{1,128}$ is then given by $R_{1,128} = R_{2,128}(R_1/R_c)(R_2/R_c)^{-1}$, and is listed in Table 5 for our eight models. The velocity of the forward shock at 128 yr is given by $V_{1,128} = V_{\text{ej,max}}(128 \text{ yrs})(R_1/R_c)(R_2/R_c)^{-1}(n-3)n^{-1}$, and is also listed in Table 5. In their models, S. K. Sarbadhicary et al. (2019) assumed 12,500 km s⁻¹ as a lower limit to the velocity of the outer shock, which (for $n = 10$) would require $V_{\text{ej,max}}(128 \text{ yr}) \approx 15,250$ km s⁻¹, i.e., faster ejecta than observed by R. A. Fesen et al. (2017). For the sake of completeness, we also list in Table 5 the velocity of the reverse shock, where we made use of the ratio of fluid velocities of shocked ejecta and shocked ISM at their respective shock fronts as given by R. A. Chevalier (1982).

The amount of swept-up ejecta by the reverse shock at t_b is $M_2(t_b) = (3-a)(n-a)^{-1}M$, and at 128 yr, the corresponding mass, $M_{2,128}$, is a fraction $(0.9/1.34)^{(n-3)}$ smaller. The mass of ISM swept up by the forward shock is given by $M_{1,128} = M_{2,128}(M_2/M_1)^{-1}$, where the M_2/M_1 ratio is taken from R. A. Chevalier (1982). The density of the unshocked ISM is then found from

$$n_{\text{H}} = 0.171 \frac{M_{1,128}}{m_p R_{1,128}^3} \text{ cm}^{-3}, \quad (3)$$

and $t_b = 128 (1.34/0.9)^{n/3}$ yr. The general dependence on t_b is $t_b \propto \rho_{\text{ISM}}^{-1/3} M^{5/6} E^{-1/2}$. The case with $a = 0$, $n = 7$, $E_{51} = 1$, $M = 1.4 M_{\odot}$, and $n_{\text{H}} = 1 \text{ cm}^{-3}$, for which $t_b \approx 204$ yr, was discussed in R. A. Chevalier (1982). For $n = 10$, and other parameters being the same as in R. A. Chevalier (1982), $t_b \approx 232$ yr. This case was studied by S. K. Sarbadhicary et al. (2019) for SN 1885A. We find larger values for t_b (Table 5), and it seems the remnant will remain in its free-expansion phase for at least another ~ 2 centuries.

3.1.1. Radio

To model the radio emission from the interaction between the ejecta and the ISM, we assume that a fraction ϵ_B of the forward shock energy density, $\rho_{\text{ISM}} V_1^2$, goes into magnetic field energy density, u_B , and a fraction ϵ_{rel} goes into relativistic electron energy density, u_{rel} .

Table 4
Other Sources in the M31 Core—Radio Fluxes from This Work

Source	R.A.	Decl.	Central Frequency (GHz)	Integrated Flux Density (mJy)	Major (arcsec)	Minor (arcsec)	PA (deg)
GLG 001/37W 142	00 ^h 42 ^m 45. ^s 21	41 ^d 15 ^m 05. ^s 58	0.145 3	9.1 ± 0.6 1.2 ± 0.01	7.1 ± 0.3 0.55 ± 0.001	6.8 ± 0.3 0.53 ± 0.001	82.1 ± 49.7 68.6 ± 2.3
M31N 2010-04a	00 ^h 42 ^m 44. ^s 97	41 ^d 15 ^m 09. ^s 47	0.145 3	20.7 ± 2.9 0.1 ± 0.01	12.4 ± 3.3 0.6 ± 0.02	7.6 ± 1.5 0.52 ± 0.02	125.8 ± 25.8 179.5 ± 10.2
CXOU J004249.11 +411456.6	00 ^h 42 ^m 49. ^s 12	41 ^d 14 ^m 56. ^s 48	3	0.04 ± 0.01	0.76 ± 0.13	0.74 ± 0.13	145.7 ± 0.01
M31*	00 ^h 42 ^m 44. ^s 32	41 ^d 16 ^m 08. ^s 43	3	0.028 ± 0.006	0.71 ± 0.11	0.52 ± 0.06	178.2 ± 21.3
2CXO J004245.1+411659	00 ^h 42 ^m 45. ^s 17	41 ^d 16 ^m 59. ^s 16	3	0.04 ± 0.008	0.8 ± 0.1	0.6 ± 0.07	109.6 ± 23

Note. For cross-identifications and references, the reader is referred to the NASA/IPAC Extragalactic Database.

For the relativistic electrons, we assume a power-law distribution of the electron energies, $n(\varepsilon) = N_0 \varepsilon^{-p}$, where $\varepsilon = \gamma m_e c^2$ is the energy of the electrons and γ is the Lorentz factor. From this one finds that

$$N_0 = \epsilon_{\text{rel}}(p-2)\rho_{\text{ISM}}V_1^2(\gamma_{\text{min}}m_e c^2)^{p-2}, \quad (4)$$

where $\gamma_{\text{min}}m_e c^2$ is the minimum energy of electrons contributing to the synchrotron emission. The parameter N_0 can also be expressed as

$$N_0 = f_{\text{rel}}(p-1)n_{e,1}(\gamma_{\text{min}}m_e c^2)^{p-1}, \quad (5)$$

where $n_{e,1}$ is the postshock electron density at the forward shock and $f_{\text{rel}} = n_{\text{rel},1}/n_{e,1}$. Here, $n_{\text{rel},1}$ is the density of the postshock electrons with $\gamma \geq \gamma_{\text{min}}$ with the condition that $\gamma_{\text{min}} \geq 1$. η is the shock compression factor (taken to be $\eta = 4$) and

$$\mu_e = \frac{1 + 4 \frac{n_{\text{He}}}{n_{\text{H}}}}{1 + 2 \frac{n_{\text{He}}}{n_{\text{H}}}}. \quad (6)$$

Equations (4) and (5) give

$$\gamma_{\text{min}} = \left(\frac{p-2}{p-1} \right) \left(\frac{m_p}{m_e} \right) \left(\frac{\epsilon_{\text{rel}} \mu_e}{\eta f_{\text{rel}}} \right) \left(\frac{V_1}{c} \right)^2, \quad (7)$$

but because f_{rel} is unknown we have chosen to initially put $f_{\text{rel}} = 1$ in Equation (7) and call this γ -value γ_{min_1} . We then estimate γ_{min} from

$$\gamma_{\text{min}} = \max(1, \gamma_{\text{min}_1}), \quad (8)$$

and estimate f_{rel} from

$$f_{\text{rel}} = \frac{\gamma_{\text{min}_1}}{\gamma_{\text{min}}} \quad (9)$$

(see also C. E. Harris et al. 2023).

We have used $\epsilon_{\text{rel}} = 0.001$, which is close to the geometric mean of 9.5×10^{-4} for the young Type Ia SNRs Tycho, Kepler, and G1.9+0.3 (S. P. Reynolds et al. 2021). For this low value of ϵ_{rel} , $\gamma_{\text{min}} = 1$ (see Equation (7)) and $f_{\text{rel}} < 1$ (see also C. E. Harris et al. 2023). Table 5 lists f_{rel} at 128 yr for our eight models. Note that f_{rel} does not explicitly depend on density. For p we have selected $p = 2.3$, which is within the range $p \in$

[2.2, 2.5] typical for SNRs (e.g., D. A. Green 2019), but we note that for the specific case of G1.9+0.3, $p \approx 2.6$ (K. J. Luken et al. 2020, see also Section 3.1.3).

For the postshock magnetic field energy density, $B = (8\pi u_B)^{1/2}$, and in Table 5 we list B at 128 yr for our models assuming $\epsilon_B = 0.01$. The values of B for models M1, M2, and M7 are similar to those of Kepler, Tycho, and G1.9+0.3, which have a geometric mean of 229 μG (S. P. Reynolds et al. 2021). The values for RX J1713.7-3946, RCW 86, and SN 1006 are $\sim 100 \mu\text{G}$, and thus close to the values for our models M3 and M4. It therefore seems that $\epsilon_B = 0.01$ is of the right order and it also agrees with the geometric mean of $\epsilon_B \approx 0.017$ for Tycho, Kepler, and G1.9+0.3 (S. P. Reynolds et al. 2021). S. K. Sarbadhary et al. (2019) devised a complete analytical approach to estimate the evolution of ϵ_B , but since we are mainly interested in only one epoch (at ~ 130 yr), and since the method does not reproduce observed radio emission for individual SNRs (D. A. Leahy et al. 2022), we have used a fixed value for ϵ_B .

The intensity of optically thin synchrotron emission is $\propto \nu^{-\alpha}$, where $\alpha = (p-1)/2$. For $p = 2.3$, $\alpha = 0.65$. If we include synchrotron self-absorption (SSA), the radio luminosity L_ν can be written as,

$$L_\nu = 4\pi^2 R_1^2 \frac{c_5}{c_6} B^{-1/2} \left(1 - \exp \left[- \left(\frac{\nu}{\nu_1} \right)^{-(p+4)/2} \right] \right) \left(\frac{\nu}{2\nu_1} \right)^{5/2} \text{ erg s}^{-1} \text{ Hz}^{-1}. \quad (10)$$

Optical depth unity occurs at the frequency ν_1 given by

$$\nu_1 = 2c_1 (s c_6 N_0)^{2/(p+4)} B^{(p+2)/(p+4)} \text{ Hz}. \quad (11)$$

The constants c_1 , c_5 , and c_6 are from A. G. Pacholczyk (1970) and have the values (in cgs units) 6.27×10^{18} , 9.68×10^{-24} , and 8.1×10^{-41} , respectively. s is the thickness of a cylindrical slab such that

$$\pi R_1^2 s = \frac{4\pi R_1^3}{3} \left[1 - \left(\frac{R_2}{R_1} \right)^3 \right] \text{ cm}^3. \quad (12)$$

The volume of synchrotron emission is assumed to be the entire volume between the reverse and forward shocks.

Table 5
Model Parameters for SN 1885A

Model	n	a	E (10^{51} erg)	n_{H} (cm^{-3})	t_{b} (yr)	$M_{1,128}$ (M_{\odot})	$R_{1,128}$ (pc)	$V_{1,128}$ (km s^{-1})	$V_{2,128}$ (km s^{-1})	B_{128}^{a} (μG)	$f_{\text{rel},128}^{\text{b}}$ $\times 10^{-4}$	$L(150 \text{ MHz})_{133}^{\text{a,b}}$ ($\times 10^{22}$ $\text{erg s}^{-1} \text{Hz}^{-1}$)
M1	7	0	1.35	0.155	324	0.244	2.22	9670	4310	292	1.28	232
M2	7	1	1.13	0.121	324	0.190	2.22	9670	4310	258	1.28	147
M3	10	0	0.95	0.0188	482	0.024	2.05	10,980	3020	115	1.66	4.81
M4	10	1	0.79	0.0140	482	0.017	2.05	10,980	3020	99	1.66	2.80
M5	12	0	0.87	0.0051	629	0.0061	2.02	11,570	2510	63	1.87	0.48
M6	12	1	0.72	0.0037	629	0.0044	2.02	11,570	2510	54	1.87	0.27
M7	8	0	1.13	0.0722	370	0.101	2.13	10,170	3760	210	1.42	54.7
M8	9	0	1.02	0.0352	422	0.046	2.08	10,610	3350	153	1.54	14.8

Notes.

^a Evaluated for $\epsilon_B = 0.01$.

^b Evaluated for $\epsilon_{\text{rel}} = 0.001$ and $p = 2.3$.

The evolution of the modeled luminosities for 150 MHz and 6.2 GHz for models M1–M6 and M8 is shown in Figure 3. For all the models, $\nu_1 \ll 150$ MHz even just one year after explosion, indicating optically thin emission, so SSA is unimportant for SN 1885A. The observed upper limits of $3.46 \times 10^{23} \text{ erg s}^{-1} \text{ Hz}^{-1}$ at 150 MHz and 133 yr, and $8.43 \times 10^{21} \text{ erg s}^{-1} \text{ Hz}^{-1}$ at 6.2 GHz and 127 yr, are marked in the figure. The 150 MHz luminosities for the models are listed in Table 5. The 6.2 GHz limit is the most constraining and SN 1885A would have been detected at 6.2 GHz if similar to models M1, M2, and M8, and at 150 MHz if similar to M1 and M2. For $p > 3$, the LOFAR data would have been more constraining than the 6.2 GHz data.

The modeled emission is sensitive to the parameter n , but insensitive to a . With the choices of $\epsilon_{\text{rel}} = 0.001$, $\epsilon_B = 0.01$, $p = 2.3$, and a structure similar to that of the explosion model 5p02822.16 (P. Höflich et al. 2002), $n \gtrsim 9$, $n_{\text{H}} \lesssim 0.035 \text{ cm}^{-3}$, and $E_{51} \lesssim 1$. S. K. Sarbadhickey et al. (2019) assumed $n = 10$, a fixed value for V_1 at 128 yr of $12,500 \text{ km s}^{-1}$, $p = 2.2$, and $\epsilon_{\text{rel}} = 0.0001$. They arrive at $n_{\text{H}} \lesssim 0.04 \text{ cm}^{-3}$, which our model M3 confirms if we artificially increase V_1 and ϵ_B , and decrease ϵ_{rel} to similar values to those of S. K. Sarbadhickey et al. (2019). In our analysis, what is new is that we tie n_{H} to a modeled ejecta structure with n added for the outermost ejecta. We also note here that the low values of n_{H} found in the radio modeling of SN 1885A matches well with observations that find the central region of M31 devoid of gas (R. Braun et al. 2009; A. L. Melchior & F. Combes 2011).

Although not shown in Figure 3, the 6.2 GHz luminosity at 127 yr ($< 8.43 \times 10^{21} \text{ erg s}^{-1} \text{ Hz}^{-1}$) is similar to that in model M7 (which has $n = 8$) if we change from $p = 2.3$ to $p = 2.6$. In this $n = 8$ model, $n_{\text{H}} = 0.072 \text{ cm}^{-3}$ and $E_{51} = 1.13$ (i.e., close to that in the 5p02822.16 model). The choice of $p = 2.6$ is motivated by the p -value for the spatially integrated emission in G1.9+0.3 (K. J. Luken et al. 2020, see Section 3.1.3.). In summary, with $M = 1.4 M_{\odot}$, $p = 2.3$, and our preferred values of ϵ_{rel} and ϵ_B , we do agree with S. K. Sarbadhickey et al. (2019) on the upper limit of $n_{\text{H}} \lesssim 0.04 \text{ cm}^{-3}$, but for the larger value of $p = 2.6$, $n_{\text{H}} \lesssim 0.07 \text{ cm}^{-3}$. For these two choices of values for p , $n \gtrsim 9$ and $n \gtrsim 8$, respectively. The latter model can accommodate $E_{51} = 1.1$, which agrees with the kinetic energy in the 5p02822.16 model (P. Höflich et al. 2002), but our limit on E is only $\approx 10\%$ lower for $p = 2.3$ and $n \gtrsim 9$.

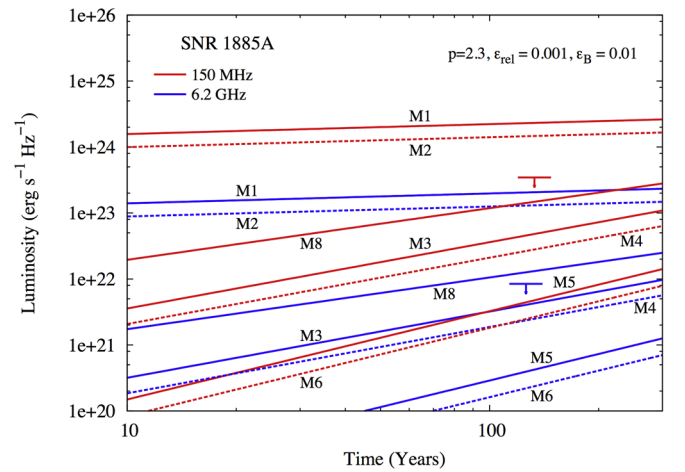


Figure 3. SN 1885A at 150 MHz (red lines) and 6.2 GHz (blue). Observed upper limits at 127 yr (for 6.2 GHz) and 133 yr (for 150 MHz) are marked, as well as the modeled evolution for models M1–M6 and M8 in Table 5. For all models, we have assumed the parameters $\epsilon_{\text{rel}} = 0.001$, $\epsilon_B = 0.01$, and $p = 2.3$.

3.1.2. X-Rays

F. Hofmann et al. (2013) obtained 28 X-ray counts in the range 0.2–10 keV at the position of SN 1885A, extracted from a 1.02 Ms merged Chandra image. They note that this is a 2.6σ significance but not a clear detection for SN 1885A. We have used an average age of 123 yr for SN 1885A for this data. Source counts were also given for the nearby remnants Braun 80, Braun 95, and Braun 101 from the same image with the counts 446, 731, and 856, respectively. The respective significance of the source detections are 3.2σ , 4.5σ , and 6.7σ . In Table 1 (available at the CDS via Vizier), F. Hofmann et al. (2013) translate source counts into luminosity for Braun 101, and obtain $6.2 \pm 0.49 \times 10^{35} \text{ erg s}^{-1}$ for a presumed spectrum of $L_{\nu} \propto \nu^{-0.7}$, a column density of foreground material $N_{\text{H}} = 6.6 \times 10^{20} \text{ cm}^{-2}$, and a distance to the remnant of 780 kpc. For similar spectra and column densities for the other remnants, this would mean 0.2–10 keV luminosities of $\sim 3.2 \times 10^{35} \text{ erg s}^{-1}$, $\sim 5.3 \times 10^{35} \text{ erg s}^{-1}$, and $\lesssim 2.0 \times 10^{34} \text{ erg s}^{-1}$ for Braun 80, Braun 95, and SN 1885A, respectively. Here, we have treated the 2.6σ tentative detection for SN 1885A as an upper limit.

The 0.2–10 keV luminosities for Braun 95 and Braun 101 can be compared with the 0.3–7 keV luminosities estimated by

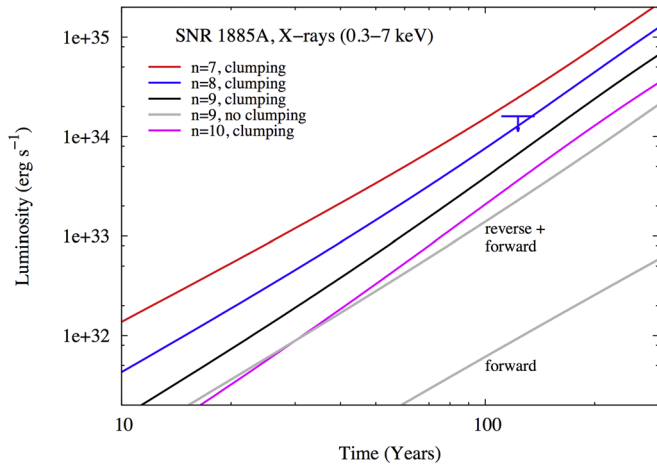


Figure 4. Evolution of the thermal X-ray luminosity between 0.3 and 7 keV for SN 1885A for models with values of n between 7 and 10 (see Table 6). The uppermost gray line is for model M8 with emission coming from both the forward and reverse shocks. The forward shock contribution is shown by the lowermost gray line. For the models shown by the other lines clumping of the shocked supernova ejecta has been assumed. The upper limit is for a luminosity of $1.6 \times 10^{34} \text{ erg s}^{-1}$ at 123 yr. See text for further details.

A. K. H. Kong et al. (2003) who obtained $8_{-2.2}^{+7.0} \times 10^{35} \text{ erg s}^{-1}$ and $4.4_{-2.2}^{+1.3} \times 10^{35} \text{ erg s}^{-1}$ for Braun 95 and Braun 101, respectively, from 37.7 ks Chandra Advanced CCD Imaging Spectrometer data. They assumed 0.26 keV (Braun 95) and 0.25 keV (Braun 101) thermal spectra and $N_{\text{H}} = 10^{21} \text{ cm}^{-2}$, and for Braun 90 they included a power-law component with $L_{\nu} \propto \nu^{-\alpha_{\nu}}$, with $\alpha_{\nu} = 1.16_{-2.16}^{+1.39}$. For Braun 101 they also analyzed 50 ks of 0.3–7 keV Chandra High Resolution Camera data and estimated $(7.1 \pm 2.5) \times 10^{35} \text{ erg s}^{-1}$ for the same spectral model and N_{H} as for the 37.7 ks data. Considering the spectral range and assumed spectral shape by F. Hofmann et al. (2013), their 0.2–10 keV luminosities would be $\sim 26\%$ lower if limited to the 0.3–7 keV range, i.e., $\sim 4.9 \times 10^{35} \text{ erg s}^{-1}$ for Braun 101. This is compatible with the results of A. K. H. Kong et al. (2003), whereas for Braun 95 the agreement is worse. There are two XMM-Newton studies that detect Braun 101 as well (see Table 2). While a luminosity of $6.0 \times 10^{35} \text{ erg s}^{-1}$ reported for Braun 101 in H. Stiele et al. (2011) for 0.2–4.5 keV matches well with the luminosity of $6.2 \times 10^{35} \text{ erg s}^{-1}$ found by F. Hofmann et al. (2013), a much higher luminosity of $1.2 \times 10^{36} \text{ erg s}^{-1}$ for the 0.35–2 keV range is reported in M. Sasaki et al. (2012), which seems to be an outlier in comparison.

For SN 1885A, the 0.3–7 keV luminosity would be $\lesssim 1.6 \times 10^{34} \text{ erg s}^{-1}$ (if it is 26% lower than for the 0.2–10 keV range), we have marked this upper limit in Figure 4. The X-ray emission from SN 1885A can be thermal and/or nonthermal. For example, both G1.9+0.3 and Tycho have a combination of both (e.g., K. J. Borkowski et al. 2013; A. Ellien et al. 2023), but with a dominance of nonthermal synchrotron emission, although inverse Compton scattering could possibly contribute for G1.9+0.3 (M. A. Villagran et al. 2024). In particular, G1.9+0.3, which is of similar age as SN 1885A, had in 2009 a total 1–7 keV luminosity of $\sim 2.4 \times 10^{34} \text{ erg s}^{-1}$ (evaluated from A. K. Carlton et al. 2011 and a distance of 8.5 kpc to the remnant), i.e., close to our likely upper limit for SN 1885A. A detailed comparison between SN 1885A and G1.9+0.3 is provided in Section 3.1.3.

Table 6

SN 1885A: Ion Density, Temperature (at 123 yr), and Filling Factor for Shocked ISM and Supernova Ejecta

n (Model ^a)	$n_{\text{ion},1}$ ^b (cm^{-3})	$n_{\text{ion},2}$ ^c (cm^{-3})	$T_{1,123}$ (10^8 K)	$T_{2,123}$ (10^8 K)	$\xi_{V,1}$	$\xi_{V,2}$
7 (M1)	0.682	0.0376	13.4	8.19	0.64	0.87
8 (M7)	0.318	0.0283	14.8	6.22	0.72	0.91
9 (M8)	0.155	0.0204	16.0	4.91	0.77	0.96
10 (M3)	0.0823	0.0151	17.1	3.98	0.81	0.94

Notes.^a Models are described in Table 5.^b Ion density of shocked ISM assuming $n_{\text{He}}/n_{\text{H}} = 0.1$.^c Ion density of shocked supernova ejecta assuming $n_{\text{S}}/n_{\text{Si}} = 1$.

To judge whether thermal emission could play an important role for SN 1885A, we note that it is set by the temperature, density, and abundances of the shocked ejecta and shocked ISM. The temperature is given by

$$T = 2.27 \times 10^9 \mu_s V_4^2 \text{ K}, \quad (13)$$

where μ_s is the mean molecular weight per particle (for both electrons and ions), and V_4 the shock velocity in 10^4 km s^{-1} . For fully ionized plasma with $n_{\text{He}}/n_{\text{H}} = 0.1$, $\mu_s = 0.61$, which applies to the shocked ISM. For the shocked ejecta (guided by the explosion model 5p02822.16 by P. Höflich et al. 2002), we assume that they only consist of silicon and sulfur with equal number densities, which results in $\mu_s = 1.88$ for fully ionized plasma. The shock temperatures of the forward and reverse shocks at 123 yr are given in Table 6 for models with $a = 0$ and n in the range 7–10. In the same table, we also give the number densities of the ions of the shocked media ($n_{\text{ion},1}$ and $n_{\text{ion},2}$) where we have used ratio of ρ_2/ρ_1 (i.e., the reverse shock to forward shock density ratio) from the similarity solutions of R. A. Chevalier (1982).

To calculate the thermal X-ray emission, we assume that the density is constant within the volumes of shocked ISM and shocked ejecta, which we name \mathbb{V}_1 and \mathbb{V}_2 , respectively. Similarity solutions (R. A. Chevalier 1982) show that the density is not really constant, and we have therefore introduced the filling factor $\xi_{V,2}$ so that the amount of swept-up mass for the ejecta, M_2 , agrees with the similarity solutions, i.e., $M_2 = \rho_2 \xi_{V,2} \mathbb{V}_2$, and likewise for the forward shock $M_1 = \rho_1 \xi_{V,1} \mathbb{V}_1$. As can be seen from Table 6, the filling factors are close to unity, especially for the shocked ejecta, which is the region which is likely to dominate the thermal X-ray emission (see below). For the temperature, we presume that this is also constant within the shocked regions, but we have chosen to fix the electron temperature, T_e , at 20% of the shock temperature, in line with, e.g., models for the late X-ray emission of SN 1993J (P. Chandra et al. 2009; E. Kundu et al. 2019) and for the Tycho SNR (U. Hwang et al. 2002). To numerically calculate the thermal X-ray emission, we utilize the plasma code used in E. Kundu et al. (2019) and described in some detail in E. I. Sorokina et al. (2004). It includes the elements H, He, C, N, O, Ne, Na, Mg, Al, Si, S, Ar, Ca, Fe, and Ni. For the shocked ISM, we assume $n_{\text{He}}/n_{\text{H}} = 0.1$ and for the other elements we choose solar abundances as given by E. Magg et al. (2022).

In Figure 4, we show the evolution between 10 and 300 yr of the thermal X-ray luminosity between 0.3 and 7 keV for

models with $n \in [7, 10]$ and $a = 0$. The upper gray line is for model M8 (i.e., $n = 9$) and shows the dominance of the reverse shock over the forward shock (portrayed by the lower gray line). The electron temperature of the reverse shock in this model is ≈ 8.5 keV, and the 0.3–7 keV luminosity is almost an order of magnitude below the observed X-ray upper limit. Recapitulating from Section 3.1.1, this model (with $p = 2.3$) gives a radio luminosity at 6.2 GHz that is close to the observed upper limit at that frequency (see Figure 3).

In order for thermal emission within the 0.3–7 keV range to be more efficient one can invoke clumping, which could be the result of inhomogeneous ejecta. For the four models with clumping in Figure 4 we have assumed that for one-sixth of $\xi_{V,2} \mathbb{V}_2$ the shocked ejecta are a factor of 8/3 denser than $n_{\text{ion},2}$ in Table 6 and that the remaining five-sixths of $\xi_{V,2} \mathbb{V}_2$ has a density that is four times lower than in the clumps. This preserves the mass M_2 compared to the nonclumped models in Table 6. The shocked ejecta are assumed to be in pressure equilibrium so that the temperature changes inversely with density. For the $n = 9$ model (black line in Figure 4) this results in a factor of ≈ 3 higher luminosity at 123 days compared to the model with no clumping, but still a factor ~ 2.4 lower than the observed upper limit. So, clumping even by this amount is fully compatible with our estimated upper limit of luminosity within the 0.3–7 keV range. If we were to treat the Chandra data as a tentative 2.6σ detection, our estimates for thermal emission indicate that nonthermal emission is expected to dominate, even if there would be significant clumping of the ejecta. However, if we allow for $p = 2.6$, the model with $n = 8$ (i.e., M7) can also pass the observational tests for both radio and X-rays, even in the case of some clumping of the shocked ejecta.

Models for thermal emission from SN 1885A were also made by H. B. Perets et al. (2011). They assume $n_{\text{H}} = 0.1 \text{ cm}^{-3}$ and $T_2 = 0.4$ keV at 125 yr. This temperature is more than an order lower than in our models and they obtain luminosities in excess of $10^{36} \text{ erg s}^{-1}$. We can reproduce this for our Model M7 (with no clumping) if we change to $T_2 = 0.4$ keV, assume solar abundances with hydrogen depressed by a factor of 10^3 and helium by a factor of 10^2 , and set $n_{\text{ion},2} = 1.0 \text{ cm}^{-3}$. (Elemental abundances are, unfortunately, not described by H. B. Perets et al. 2011.) However, luminosities from thermal X-ray emission in excess of only a few per cent of 10^{36} are at odds with the observed upper limit of SN 1885A and the observed value for G1.9+0.3. This shows the importance of using realistic temperatures and abundances.

3.1.3. Comparison to G1.9+0.3

G1.9+0.3 is between 100 and 150 yr old (K. J. Luken et al. 2020), and thus about as old as SN 1885A. Moreover, these two remnants likely both stem from Type Ia SNe. This makes a comparison between them relevant. As noted in Section 3.1.2, the 1–7 keV range luminosity for G1.9+0.3 is $\sim 2.4 \times 10^{34} \text{ erg s}^{-1}$, and the upper limit for the 0.3–7 keV range for SN 1885A is $\sim 1.6 \times 10^{34} \text{ erg s}^{-1}$. In radio, the upper limits for SN 1885A are $\sim 3.5 \times 10^{23} \text{ erg s}^{-1} \text{ Hz}^{-1}$ at 150 MHz at 133 yr and $\sim 8.4 \times 10^{21} \text{ erg s}^{-1} \text{ Hz}^{-1}$ at 6.2 GHz at 127 yr. This can be compared with the luminosities in K. J. Luken et al. (2020) for G1.9+0.3, which are $\approx 3.9 \times 10^{23} \text{ erg s}^{-1} \text{ Hz}^{-1}$ at 150 MHz and $\approx 1.9 \times 10^{22} \text{ erg s}^{-1} \text{ Hz}^{-1}$ at 6.2 GHz. Here, we have interpolated between the luminosities given by K. J. Luken et al. (2020) for 5.0 GHz and 9.0 GHz, and used a distance of

8.5 kpc to G1.9+0.3. G1.9+0.3 thus seems more luminous in both radio and X-rays than SN 1885A, and it could well have been detected both in X-rays and radio (both at 150 MHz and 6.2 GHz) had it been placed at the same distance as SN 1885A, with the clearest detection at 6.2 GHz.

In our models for SN 1885A we have assumed spherical symmetry. This agrees with the conclusion of R. A. Fesen et al. (2017) that the distribution of Ca and Mg does not support the picture of an asymmetric explosion of SN 1885A. This may also exclude a very asymmetric distribution of the ISM in the immediate vicinity of the supernova. On the contrary, G1.9+0.3 has more of a bipolar structure in X-rays, while the strongest radio emission occurs roughly orthogonal to this bipolar structure. The inferred maximum expansion along the bipolar axis is $13,600 \pm 3100 \text{ km s}^{-1}$ in radio (K. J. Luken et al. 2020), consistent with $\sim 15,000 \text{ km s}^{-1}$ in X-rays (K. J. Borkowski et al. 2017). The estimated value of n_{H} along this axis is $\sim 0.02 \text{ cm}^{-3}$ (A. K. Carlton et al. 2011). In the northwest direction, where the strongest radio emission occurs, the maximum average velocity is only $\sim 8000 \text{ km s}^{-1}$ in radio (K. J. Luken et al. 2020), and with shock speeds even less in X-rays (K. J. Borkowski et al. 2017). This could be explained by expansion into an inhomogeneous ISM (e.g., K. J. Borkowski et al. 2017), an argument that is strengthened by a molecular cloud found close the remnant by R. Enokiya et al. (2023). The bipolar structure could also be point-symmetric, and possibly signal that the supernova progenitor exploded in a planetary nebula (N. Soker 2024). An asymmetric remnant structure could also be due to the orientation of the ambient magnetic field because this affects the efficiency of how ions and electrons are accelerated round the remnant. This was discussed for SN 1006 by E. M. Reynoso et al. (2013) and D. Caprioli & A. Spitkovsky (2014).

The asymmetries for G1.9+0.3 influence the comparison to SN 1885A. For example, the radio surface brightness at 1.365 GHz (K. J. Borkowski et al. 2017) is ~ 3 –4 times higher in the northwest direction of G1.9+0.3 compared to other areas and the area of this region is ~ 3 –4 times smaller than the overall region of radio emission. This boosts the total emission by a factor of ~ 2 compared to a spherically symmetric case with a surface brightness similar to that from regions other than in the northeast. The fastest expansion of G1.9+0.3 is 30%–50% faster than in our models of SN 1885A. If we assume $p = 2.6$ (which is the global average found by K. J. Luken et al. 2020), a homogeneous ISM with $n_{\text{H}} = 0.016$, the microphysics parameters $\epsilon_B = 0.04$ and $\epsilon_{\text{rel}} = 0.001$, $n = 9$, $a = 0$, $V_b = 11,200 \text{ km s}^{-1}$, and $V_{\text{ej,max}}(128 \text{ yr}) = 17,500 \text{ km s}^{-1}$, then the modeled radio luminosity at 6.2 GHz (at 127 yr) is $\approx 1.2 \times 10^{22} \text{ erg s}^{-1} \text{ Hz}^{-1}$, i.e., $\sim 60\%$ of the observed luminosity. For this model, the rate of luminosity increase is $\sim 0.6\%$ per year. Removing emission corresponding to the northwestern region and adding the strong observed emission from that field yields a luminosity that is similar to the total overall observed emission. In this model, the forward shock advances at just below $14,000 \text{ km s}^{-1}$ in the bipolar direction, similar to the finding of A. K. Carlton et al. (2011), but the model has an explosion energy of $E_{51} = 1.7$, which is higher than expected for a Type Ia SN. A solution to this could be interaction with a density enhancement in the bipolar direction that may have started only some decades ago, as suggested by N. Soker (2024). In this case, the density inside this density enhancement could be $n_{\text{H}} < 0.016 \text{ cm}^{-3}$ (for $n = 9$) and E could be closer to the canonical 10^{51} erg . The scenario with density enhancements

is also likely to result in faster luminosity rate increase than in our homogeneous model. The observed rate is about twice as high as the $\sim 0.6\%$ per year in our model (see T. Murphy et al. 2008).

It appears as if all asymmetries in G1.9+0.3 make it a more efficient radio emitter (and presumably also in X-rays) than the seemingly more spherically symmetric SN 1885A. For a comparison, S. K. Sarbadhickey et al. (2019) used a spherically symmetric model for G1.9+0.3 and arrived at $n_{\text{H}} \approx 0.18 \text{ cm}^{-3}$. The main differences compared to us is that they assumed $p = 2.2$, a shock speed of $\sim 10,000 \text{ km s}^{-1}$, and $\epsilon_{\text{rel}} = 10^{-4}$. Their estimated density is probably more representative of that in the northeastern region than for other parts of the remnant. The value $p = 2.2$ corresponds to the average spectral index, whereas $p = 2.6$ corresponds to the luminosity-weighted spectral index (K. J. Luken et al. 2020). A more detailed modeling for G1.9+0.3 should take the spatial variation of p into account.

3.2. Braun 80, Braun 95, and Braun 101

As seen in Figures 1 and 2 we detect the SNR. Braun 80, 95, and 101 in the LOFAR image at 150 MHz and in the VLA image at 3 GHz. In radio, at 3 GHz, the sizes are $6''.17 \times 5''.55$, $6''.76 \times 5''.92$, and $6''.24 \times 5''.52$, respectively, and at 8.4 GHz $8''.0, 9''.6 \times 8''.0$, and $11''.6 \times 8''.4$, respectively (Section 2.3 and Table 1). For the three remnants, the 8.4 GHz image (L. O. Sjouwerman & J. R. Dickel 2001) gives the most reliable flux density among the frequencies used to estimate the spectral index. It has a good $0''.2$ resolution and is deeper (low noise of $4 \mu\text{Jy beam}^{-1}$), which explains the slightly larger sizes of the remnants at this frequency. This can be compared with the X-ray diameters found by F. Hofmann et al. (2013), which are $7''.8, 8''.7$, and $7''.9$, respectively. The radio and X-ray luminosities are summarized in Tables 1 and 2 (see also Section 3.1.2). Braun 80 has low surface brightness similar to the structure seen in other radio studies. Similar to what has been reported at 4.9 and 8.4 GHz by A. K. H. Kong et al. (2003), Braun 101 has a northeastern side that is three times brighter than the southwestern side ($0.47 \text{ v } 0.16 \text{ mJy}$) in the 3 GHz image. Braun 95 has a very apparent shell-like structure.

To estimate the properties of the remnants, we use the empirical expression of D. A. Leahy et al. (2022) for the radio luminosity at 1.4 GHz

$$L_{1.4} \approx 2.3 \times 10^{24} \left(\frac{n_{\text{ISM}}}{1 \text{ cm}^{-3}} \right)^{0.85} \left(\frac{R_s}{10 \text{ pc}} \right)^{2.1} \left(\frac{V_s}{500 \text{ km s}^{-1}} \right)^{1.3} \text{ erg s}^{-1} \text{ Hz}^{-1}. \quad (14)$$

If the remnants are in the Sedov phase, their radii and shock velocities can be described by

$$R_s \approx 12.5 t_4^{0.4} E_{51}^{0.2} n_{\text{ISM}}^{-0.2} \text{ pc} \quad (15)$$

$$V_s \approx 490 \left(\frac{R_s}{12.5 \text{ pc}} \right) t_4^{-1} \text{ km s}^{-1}, \quad (16)$$

respectively (S. K. Sarbadhickey et al. 2017). Here, t_4 is the age in 10^4 yr . For $E_{51} = 1.0$ and $n_{\text{ISM}} = 0.1 \text{ cm}^{-3}$ (as guided by Z. Li et al. 2009), and radii inserted from the major axes of the 8.4 GHz images, Equations (15) and (16) give $t_4 \approx 0.52$ (0.81, 1.31) and $V_s \approx 1150, (880, 660) \text{ km s}^{-1}$ for Braun 80 (Braun 95, Braun 101), where the age is $\propto (n_{\text{ISM}}/E)^{1/2}$. Including SN 1885A and possibly undetected supernovae, this would indicate one supernova

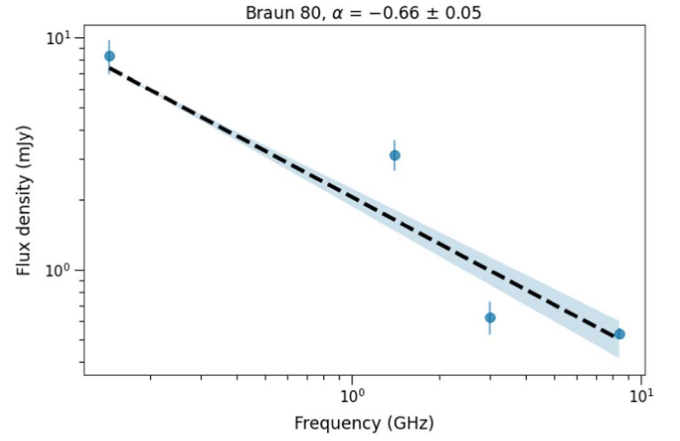


Figure 5. Spectra of Braun 80.

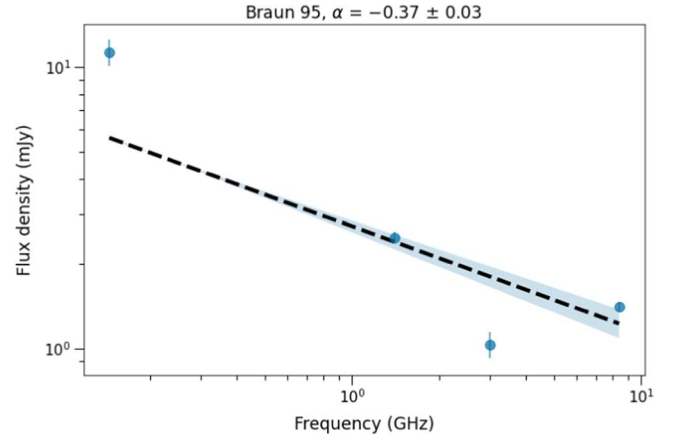


Figure 6. Spectra of Braun 95.

explosion every $\lesssim 3000 (n_{\text{ISM}}/0.1)^{0.5} (E_{51,m})^{-0.5} \text{ yr}$ in this central $0.5 \text{ kpc} \times 0.6 \text{ kpc}$ region, where $E_{51,m}$ is the reciprocal mean of the kinetic energies of the remnants in 10^{51} erg .

We can now use Equation (14) to estimate the expected radio luminosity at 1.4 GHz from the derived values for R_s and V_s , as well as the assumed value for $n_{\text{ISM}} = 0.1 \text{ cm}^{-3}$, and we find $L_{1.4} \approx 2.3 (2.4, 2.5) \times 10^{24} \text{ erg s}^{-1} \text{ Hz}^{-1}$ for Braun 80 (Braun 95, Braun 101). In D. A. Leahy et al. (2022) there are 31 out of 58 SNRs with shock velocities between 600 and 1200 km s^{-1} and known luminosity at 1.4 GHz, and their median value of $L_{1.4}$ is $\approx 1.0 \times 10^{24} \text{ erg s}^{-1} \text{ Hz}^{-1}$. This can be compared with the observed luminosities at 1.4 GHz for Braun 80 (Braun 95, Braun 101) which are $L_{1.4} \approx 2.3 (1.8, 2.2) \times 10^{24} \text{ erg s}^{-1} \text{ Hz}^{-1}$. In addition, from the derived spectral indices in Figures 5, 6, and 7, the estimated luminosities at 1.4 GHz for Braun 80 (Braun 95, Braun 101) are $L_{1.4} \approx 1.2 (1.7, 1.8) \times 10^{24} \text{ erg s}^{-1} \text{ Hz}^{-1}$.

The VLA observations are at much better resolutions compared to the LOFAR image and all three remnants are resolved in all other frequencies except at 150 MHz. The spectral indices estimated in Figures 5, 6, and 7 have some caveats because the scales covered by these images at different resolutions may not match very well. The 3 GHz VLA image covers scales from $0''.5$ to $18''$, the 8.4 GHz images covers $0''.2$ – $20''$, and the 150 MHz image covers $6''$ to several arcminutes. The 1.4 GHz image has a lower resolution ($5''$) and is also expected to have some confusion from the extended background. At 8.4 GHz, the fluxes reported for these remnants

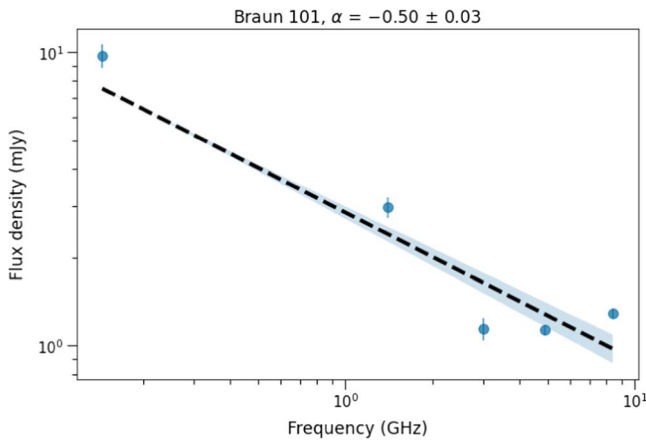


Figure 7. Spectra of Braun 101.

are only partially recovered in L. O. Sjouwerman & J. R. Dickel (2001) because large scale diffuse emission greater than $10''$ are filtered out, as explained in L. O. Sjouwerman et al. (2005). Given these caveats, the spectral indices of the remnants (-0.66 ± 0.05 , -0.37 ± 0.03 , and -0.5 ± 0.03 for Braun 80, 95, and 101, respectively) match fairly well with those found in previous studies (A. K. H. Kong et al. 2003; L. O. Sjouwerman & J. R. Dickel 2001). A. K. H. Kong et al. (2003) mention that the flux density measured at 1.4 GHz might be confused with the extended background but derive a spectral index of -0.77 for Braun 80. L. O. Sjouwerman & J. R. Dickel (2001) find spectral index of -0.3 and -0.5 for Braun 95 and 101, respectively, while adopting a nominal -0.5 for Braun 80 due to the confused flux densities. As noted in the captions, 3% errors were used for the 8.4 and 4.9 GHz fluxes to estimate the spectral indices. This is because only the noise level is reported in L. O. Sjouwerman & J. R. Dickel (2001) and A. K. H. Kong et al. (2003). We note here also that the indices are sensitive to these error assumptions. For example, for 1% error assumed in addition to the 3σ noise, the indices then become -0.64 ± 0.05 , -0.3 ± 0.03 , and -0.1 ± 0.03 for Braun 80, 95, and 101, respectively. The difference for Braun 101 is due to the dominance of the 4.9 GHz and 8.4 GHz measurements in this case.

4. Conclusion

We presented the first LOFAR image of the center of M31 at a resolution of $6''$ and rms of $0.1 \text{ mJy beam}^{-1}$ at a 150 MHz. Along with this, we used a 3 GHz VLA image with a beam size of $0''.5$ and rms of $3 \mu\text{Jy beam}^{-1}$, and previously published radio and X-ray data to study four remnants in this central region of M31 (SN 1885A, and Braun 80, 95, and 101).

In our models for the historical SN 1885A, we assume spherically symmetric ejecta that expand homologously and density structure that can be approximated by two power laws: $\rho_i(V, t) \propto V^{-a}t^{-3}$ and $\rho_o(V, t) \propto V^{-n}t^{-3}$, where a and n correspond to the slopes of the inner and outer ejecta structure, respectively. Using values guided by previous studies of SN 1885A, and the similarity solutions of R. A. Chevalier (1982), we model the SN ejecta for a -values 0 and 1 and n -values 7–12 to approximate the full density profile. We estimate time t_b , which gives the age at which SN 1885A is expected to transition to the Sedov–Taylor stage. We find larger values of t_b than previously estimated, indicating that the remnant will stay

in the free-expansion phase for at least another couple of centuries.

We also perform radio modeling using our upper limit at 150 MHz and the upper limit at 6.2 GHz in S. K. Sarbadhickey et al. (2019). We use $\epsilon_{\text{rel}} = 0.001$ and $\epsilon_B = 0.01$ which are close to the geometric means of SNRs Tycho, Kepler, and G1.9+0.3. We also assume the spectral index for the power-law distribution of synchrotron-emitting electrons to be $p = 2.3$, which is within the range typical for SNRs. For models with $n \in [7, 9]$, we obtain postshock magnetic field energy density values of B similar to $B = 229 \mu\text{G}$ which is the geometric mean for the remnants Tycho, Kepler, and G1.9+0.3. For models with $n \in [10, 12]$, B is closer to $100 \mu\text{G}$, which is similar to the B -values found for RX J1713.7-3946, RCW 86, and SN 1006. The 6.2 GHz data (S. K. Sarbadhickey et al. 2019) is the deepest radio image obtained at the position of SN 1885A and is the most constraining for our models. Emission at 6.2 GHz would have been observed if similar to our models M1, M2, and M8, and detectable at 150 MHz if similar to the models M1 and M2. For a spectral index of $p = 2.3$ for the relativistic electrons, we agree with S. K. Sarbadhickey et al. (2019) on the upper limit of $n_H \lesssim 0.04 \text{ cm}^{-3}$. For the steeper index $p = 2.6$, the limit is $n_H \lesssim 0.07 \text{ cm}^{-3}$. For these two choices of values for p , $n \gtrsim 9$ and $n \gtrsim 8$, respectively. The latter model can accommodate $E_{51} = 1.1$, which agrees with the kinetic energy in the 5p02822.16 model (P. Höflich et al. 2002), but our limit on E is only $\approx 10\%$ lower for $p = 2.3$ and $n \gtrsim 9$.

F. Hofmann et al. (2013) report a 2.6σ significance for SN 1885A in X-ray data from deep Chandra imaging at 0.2–10 keV. We estimate a luminosity value of $\lesssim 2.0 \times 10^{34} \text{ erg s}^{-1}$ from their reported source count. We treat this as an upper limit for modeling the X-ray emission and check if thermal emission would play a significant role. Even if clumping of the ejecta is invoked for more efficient thermal emission, we find that nonthermal emission is expected to dominate the X-ray emission.

We then compare our results on SN 1885A with those on G1.9+0.3. We use the luminosities at 5 GHz and 9 GHz reported by K. J. Luken et al. (2020), and interpolate these values to 150 MHz and 6.2 GHz using a distance of 8.5 kpc for G1.9+0.3. We find that, had G1.9+0.3 been at the same distance as SN 1885A, it could very well have been detected not only at 6.2 GHz but also at 150 MHz. While we assume spherical symmetry for SN 1885A, which is supported observationally, G1.9+0.3 has asymmetries. The observed luminosity increase is about twice as high as the 0.6% per year seen in our spherically symmetric model. It appears likely that the asymmetries make G1.9+0.3 a much more efficient radio and X-ray transmitter. Further studies of the remnant should take into account these asymmetries using a spatially varying p -value (since $p = 2.2$ corresponds to an average spectral index, while $p = 2.6$ corresponds to a luminosity-weighted spectral index).

We use the 3 GHz image to characterize the SNR. Braun 80, 95, and 101, with Braun 80 having low surface brightness that affects its spectral index estimation, Braun 95 having three times more emission from the northeastern side compared to the southwestern side, and Braun 101 having a very apparent shell-like structure. We estimate two properties of the remnants, age and shock velocity, using the radii of the remnants from L. O. Sjouwerman & J. R. Dickel (2001), and assuming an explosion energy of $E_{51} = 1.0$ and an ISM density

of ($n_{\text{ISM}} = 0.1 \text{ cm}^{-3}$). We find ages of 5200, 8100, and 13,100 yr and shock velocities of 1150, 880, and 660 km s^{-1} for Braun 80, 95, and 101, respectively. For this $0.5 \text{ kpc} \times 0.6 \text{ kpc}$ central region of M31, this indicates that there is one supernova explosion every $\lesssim 3000$ yr. This result scales with the ISM density and presumed explosion energy as $\propto (n_{\text{ISM}}/E)^{1/2}$. We estimate spectral indices of -0.66 , -0.37 , and -0.5 for Braun 80, 95, and 101, respectively, which match well with the indices found by A. K. H. Kong et al. (2003) and L. O. Sjouwerman & J. R. Dickel (2001).

An SNR is expected to be brighter at lower frequencies due to optically thin power-law synchrotron emission. However, even at low frequencies of 150 MHz, SN 1885A remains undetected in the radio, as we show with LOFAR. The VLA and X-ray observations of the studied region will be difficult to push deeper with present-day facilities and techniques. However, the LOFAR data in this study can be made more sensitive using VLBI with subarcsecond resolution instead of the $6''$ data used here, as we have demonstrated for SN 2011dh in D. Venkattu et al. (2023). With a spectral index of -0.6 , which is typical for young SNRs, the expected flux density of SN 1885A at 150 MHz could be 0.1 mJy (~ 10 times higher than the upper limit at 6.2 GHz). As discussed in this work, the forward shock radius is expected to be $\approx 2 \text{ pc}$, meaning that the size of SN 1885A in radio would be $\sim 1''$ (diameter of 4 pc). Typical VLBI observations with LOFAR with $0''.3$ resolution (which is about the same as for the 6.2 GHz observations, see S. K. Sarbadhichary et al. 2019) and $\sim 80 \mu\text{Jy}$ noise level may very well be at the limit of detection for SN 1885A. Such attempts for M31 are underway (Bonnassieux et al. 2024, in preparation), and this could make the LOFAR data at least as useful as the VLA data, especially for SN 1885A.

Acknowledgments

We are grateful to the anonymous referee for the insightful comments. It is a pleasure to thank J. Moldón and M. C. Toribio for useful discussions. This paper is based on data obtained with the International LOFAR Telescope (ILT) under project code LC10_014. LoTSS Data Release 2 data are described by T. W. Shimwell et al. (2022). LOFAR data products were provided by the LOFAR Surveys Key Science project (LSKSP; <https://lofar-surveys.org/>) and were derived from observations with the International LOFAR Telescope (ILT). LOFAR (M. P. van Haarlem et al. 2013) is the Low Frequency Array designed and constructed by ASTRON. It has observing, data processing, and data storage facilities in several countries, which are owned by various parties (each with their own funding sources), and which are collectively operated by the ILT foundation under a joint scientific policy. The efforts of the LSKSP have benefited from funding from the European Research Council, NOVA, NWO, CNRS-INSU, the SURF Co-operative, the UK Science and Technology Funding Council, and the Jülich Supercomputing Centre. M.P.T. acknowledges financial support from the Severo Ochoa grant CEX2021-001131-S and from the National grant PID2020-117404GB-C21, funded by MCIU/AEI/10.13039/501100011033. The National Radio Astronomy Observatory is a facility of the National Science Foundation operated under cooperative agreement by Associated Universities, Inc. This research has made use of the NASA/IPAC Extragalactic Database (NED), which is funded by the National Aeronautics and Space Administration and operated by the California Institute of Technology.

Facilities: LOFAR, VLA.

Software: APLPY (T. Robitaille & E. Bressert 2012; T. Robitaille 2019) NUMPY (C. R. Harris et al. 2020), SCIPY (P. Virtanen et al. 2020), MATPLOTLIB (J. D. Hunter 2007), CASA (CASA Team et al. 2022), LINC (F. de Gasperin et al. 2019), DDFACET (C. Tasse et al. 2023).

ORCID iDs

Deepika Venkattu  <https://orcid.org/0000-0001-9896-6994>
 Peter Lundqvist  <https://orcid.org/0000-0002-3664-8082>
 Miguel Pérez Torres  <https://orcid.org/0000-0001-5654-0266>
 Etienne Bonnassieux  <https://orcid.org/0000-0003-2312-3508>
 Francoise Combes  <https://orcid.org/0000-0003-2658-7893>

References

- Borkowski, K. J., Gwynne, P., Reynolds, S. P., et al. 2017, *ApJL*, **837**, L7
 Borkowski, K. J., Reynolds, S. P., Hwang, U., et al. 2013, *ApJL*, **771**, L9
 Braun, R. 1990, *ApJS*, **72**, 761
 Braun, R., Thilker, D. A., Walterbos, R. A. M., & Corbelli, E. 2009, *ApJ*, **695**, 937
 Braun, R., & Walterbos, R. A. M. 1993, *A&AS*, **98**, 327
 Bystedt, J. E. V., Brinks, E., de Bruyn, A. G., et al. 1984, *A&AS*, **56**, 245
 Caprioli, D., & Spitkovsky, A. 2014, *ApJ*, **783**, 91
 Carlton, A. K., Borkowski, K. J., Reynolds, S. P., et al. 2011, *ApJL*, **737**, L22
 CASA Team, Bean, B., Bhatnagar, S., et al. 2022, *PASP*, **134**, 114501
 Chandra, P., Dwarkadas, V. V., Ray, A., Immler, S., & Pooley, D. 2009, *ApJ*, **699**, 388
 Chevalier, R. A. 1982, *ApJ*, **258**, 790
 Chevalier, R. A., & Fransson, C. 1994, *ApJ*, **420**, 268
 Chevalier, R. A., & Plait, P. C. 1988, *ApJL*, **331**, L109
 Crane, P. C., Dickel, J. R., & Cowan, J. J. 1992, *ApJL*, **390**, L9
 de Gasperin, F., Dijkema, T. J., Drabent, A., et al. 2019, *A&A*, **622**, A5
 de Vaucouleurs, G., & Corwin, H. G. J. 1985, *ApJ*, **295**, 287
 Dickel, J. R., & D’Odorico, S. 1984, *MNRAS*, **206**, 351
 Dodorico, S., Dopita, M. A., & Benvenuti, P. 1980, *A&AS*, **40**, 67
 Dwarkadas, V. V., & Chevalier, R. A. 1998, *ApJ*, **497**, 807
 Ellien, A., Greco, E., & Vink, J. 2023, *ApJ*, **951**, 103
 Enokiya, R., Sano, H., Filipović, M. D., et al. 2023, *PASJ*, **75**, 970
 Fesen, R. A., Hamilton, A. J. S., & Saken, J. M. 1989, *ApJL*, **341**, L55
 Fesen, R. A., Höflich, P. A., & Hamilton, A. J. S. 2015, *ApJ*, **804**, 140
 Fesen, R. A., Weil, K. E., Hamilton, A. J. S., & Höflich, P. A. 2017, *ApJ*, **848**, 130
 Galvin, T. J., & Filipovic, M. D. 2014, *SerAJ*, **189**, 15
 Gelfand, J. D., Lazio, T. J. W., & Gaensler, B. M. 2004, *ApJS*, **155**, 89
 Green, D. A. 2019, *JApA*, **40**, 36
 Harris, C. E., Sarbadhichary, S. K., Chomiuk, L., et al. 2023, *ApJ*, **952**, 24
 Harris, C. R., Millman, K. J., van der Walt, S. J., et al. 2020, *Natur*, **585**, 357
 Höflich, P., Gerardy, C. L., Fesen, R. A., & Sakai, S. 2002, *ApJ*, **568**, 791
 Hofmann, F., Pietsch, W., Henze, M., et al. 2013, *A&A*, **555**, A65
 Huggins, W., & Denning, W. F. 1885, *Natur*, **32**, 465
 Hunter, J. D. 2007, *CSE*, **9**, 90
 Hwang, U., Decourchelle, A., Holt, S. S., & Petre, R. 2002, *ApJ*, **581**, 1101
 Kong, A. K. H., Sjouwerman, L. O., Williams, B. F., Garcia, M. R., & Dickel, J. R. 2003, *ApJL*, **590**, L21
 Kundu, E., Lundqvist, P., Pérez-Torres, M. A., Herrero-Illana, R., & Alberdi, A. 2017, *ApJ*, **842**, 17
 Kundu, E., Lundqvist, P., Sorokina, E., et al. 2019, *ApJ*, **875**, 17
 Leahy, D. A., Merrick, F., & Filipovic, M. 2022, *Univ*, **8**, 653
 Li, Z., Wang, Q. D., & Wakker, B. P. 2009, *MNRAS*, **397**, 148
 Luken, K. J., Filipović, M. D., Maxted, N. I., et al. 2020, *MNRAS*, **492**, 2606
 Magg, E., Bergemann, M., Serenelli, A., et al. 2022, *A&A*, **661**, A140
 Magnier, E. A., Prins, S., van Paradijs, J., et al. 1995, *A&AS*, **114**, 215
 Maunder, E. W. 1885, *Obs*, **8**, 321
 Maunder, E. W. 1886, *MmSSI*, **14**, 144
 McConnachie, A. W., Irwin, M. J., Ferguson, A. M. N., et al. 2005, *MNRAS*, **356**, 979
 Melchior, A. L., & Combes, F. 2011, *A&A*, **536**, A52
 Morgan, J. S., Argo, M. K., Trott, C. M., et al. 2013, *ApJ*, **768**, 12
 Murphy, T., Gaensler, B. M., & Chatterjee, S. 2008, *MNRAS*, **389**, L23

- Pacholczyk, A. G. 1970, *Radio Astrophysics. Nonthermal Processes in Galactic and Extragalactic Sources* (San Francisco, CA: Freeman)
- Perets, H. B., Badenes, C., Arcavi, I., Simon, J. D., & Gal-yam, A. 2011, *ApJ*, **730**, 89
- Pooley, G. G., & Kenderdine, S. 1967, *Natur*, **214**, 1190
- Reynolds, S. P., Williams, B. J., Borkowski, K. J., & Long, K. S. 2021, *ApJ*, **917**, 55
- Reynoso, E. M., Hughes, J. P., & Moffett, D. A. 2013, *AJ*, **145**, 104
- Robitaille, T. 2019, APLpy v2.0: The Astronomical Plotting Library in Python v2.0, Zenodo, doi:10.5281/zenodo.2567476
- Robitaille, T., & Bressert, E., 2012 APLpy: Astronomical Plotting Library in Python, Astrophysics Source Code Library, ascl:1208.017
- Sarbadhicary, S. K., Badenes, C., Chomiuk, L., Caprioli, D., & Huizenga, D. 2017, *MNRAS*, **464**, 2326
- Sarbadhicary, S. K., Chomiuk, L., Badenes, C., et al. 2019, *ApJ*, **872**, 191
- Sasaki, M., Pietsch, W., Haberl, F., et al. 2012, *A&A*, **544**, A144
- Shimwell, T. W., Hardcastle, M. J., Tasse, C., et al. 2022, *A&A*, **659**, A1
- Sjouwerman, L. O., & Dickel, J. R. 2001, in *AIP Conf. Ser. 565, Young Supernova Remnants*, ed. S. S. Holt & U. Hwang (Melville, NY: AIP), 433
- Sjouwerman, L. O., Kong, A. K. H., Garcia, M. R., et al. 2005, in *Proc. of X-Ray and Radio Connections*, ed. L. O. Sjouwerman & K. K. Dyer (Socorro: NRAO), 4.16, <http://www.aoc.nrao.edu/events/xraydio>
- Smirnov, O. M., & Tasse, C. 2015, *MNRAS*, **449**, 2668
- Soker, N. 2024, *RAA*, **24**, 015012
- Sorokina, E. I., Blinnikov, S. I., Kosenko, D. I., & Lundqvist, P. 2004, *AstL*, **30**, 737
- Stiele, H., Pietsch, W., Haberl, F., et al. 2011, *A&A*, **534**, A55
- Supper, R., Hasinger, G., Lewin, W. H. G., et al. 2001, *A&A*, **373**, 63
- Tasse, C., Hugo, B., Mirmont, M., et al. 2018, *A&A*, **611**, A87
- Tasse, C., Hugo, B., Mirmont, M., et al., 2023 DDFacet: Facet-based Radio Imaging Package, Astrophysics Source Code Library, ascl:2305.008
- Truelove, J. K., & McKee, C. F. 1999, *ApJS*, **120**, 299
- van Haarlem, M. P., Wise, M. W., Gunst, A. W., et al. 2013, *A&A*, **556**, A2
- Venkattu, D., Lundqvist, P., Pérez Torres, M., et al. 2023, *ApJ*, **953**, 157
- Villagran, M. A., Gómez, D. O., Velázquez, P. F., et al. 2024, *MNRAS*, **527**, 1601
- Virtanen, P., Gommers, R., Oliphant, T. E., et al. 2020, *NatMe*, **17**, 261
- Walterbos, R. A. M., Brinks, E., & Shane, W. W. 1985, *A&AS*, **61**, 451